JAAS

PAPER

View Article Online
View Journal | View Issue

Cite this: J. Anal. At. Spectrom., 2015, 30, 2316

Elemental fractionation during condensation of plasma plumes generated by laser ablation: a ToF-SIMS study of condensate blankets†

Ming Tang,*[a] Ricardo Arevalo Jr.,[b] Yulia Goreva[c] and William F. McDonough[a]

Received 1st August 2015
Accepted 10th September 2015

DOI: 10.1039/c5ja00320b

www.rsc.org/jaas

Ion imaging of the condensate blanket around a laser ablation site provides a window to study elemental fractionation during condensation of a plasma plume. Here we used a Time-of-Flight Secondary Ion Mass Spectrometer (ToF-SIMS) to conduct depth profiling of the condensate blanket produced by excimer 193 nm laser ablation of NIST 610 glass. Compositional zonings (Ca normalized) revealed by ToF-SIMS are associated with texture gradients in the condensate blanket, as characterized by Secondary Electron Microprobe (SEM) images. Elements that are more volatile than Ca are relatively enriched in the inner zones (proximal to the ablation site) while more refractory elements are variable in their distributions. Volatility and ionization potential exert influence on elemental fractionation in plasma plume condensation processes as documented by the contrasting fractionation behaviors of alkaline and alkaline earth metals. Compositional zonings in the condensate blanket are due to physical and chemical zonings (*e.g.*, temperature, pressure, electron density, speciation, *etc.*) within the condensing plume as it expands and cools. Zoned condensation may be a primary mechanism driving the elemental fractionation associated with laser ablation.

Introduction

Elemental and isotopic fractionations have been documented for laser ablation (LA) of various materials[1]. Progressive localized ablation, leading to deeper incision of the sample substrate, exacerbates laser-induced fractionation and serves as one of the largest contributions to the uncertainty budget when characterizing the products of laser ablation-inductively coupled plasma-mass spectrometry (LA-ICP-MS). Chemical and isotopic fractionation during plasma condensation and particle formation should not be underestimated. Understanding these fractionation mechanisms is key to achieving high accuracy and precision in quantitative analysis using laser micro-sampling techniques such as LA-ICP-MS.

Laser processing of geological materials (insulators to conductors) involves photochemical and photothermal activation,[2] which are primarily controlled by the pulse irradiance duration of the incident laser light. Specifically, lasers with nanosecond pulse durations (the vast majority of commercial laser ablation systems) remove materials *via* inducing electronic transitions attended by significant melting and evaporation,[2] as most rocks and minerals are defined by phonon relaxation rates on the order of 10^{-12} s (*e.g.*, Bauerle, 1996). In addition to pulse duration, the ablation mechanisms are also controlled by laser wavelength[3,4] and fluence.[2,5,6] Elements with different physical (*e.g.*, volatility) and chemical (*e.g.*, electronic structure) affinities fractionate significantly during laser–matter interaction and plasma condensation.[4,7–11] Laser-induced elemental fractionation results in non-stoichiometric composition of the aerosol, which scales critically on particle size distributions.[8,12–15] Such elemental fractionation is further aggravated during aerosol transportation (particle loss) and ionization (incomplete ionization) of large particles (>~1 μm) in the ICP.[9,13,16,17] Non-stoichiometric compositions of ablated aerosols are at least partially generated from particle formation processes, of which plasma-to-particle conversion plays an important role. Plasma-to-particle conversion progresses from nucleation to condensation coalescence and agglomeration within the expanding plume.[18] These particles ultimately form a condensate blanket near the ablation site if not extracted by carrier gas.

Here we present a Time-of-Flight Secondary Ion Mass Spectrometry (ToF-SIMS) study of the condensate blanket produced by laser ablation of NIST 610 glass with nanosecond pulses of 193 nm wavelength laser radiation. ToF-SIMS is a surface-sensitive technique that uses a pulsed primary ion beam and images only the outmost (n = 1–2) atomic layers of the surface analyzed. Elements and a wide range of molecular species can be detected, though there is a wide range of sensitivities among the elements based on their first ionization potentials.[19] Ion imaging of laser condensate blankets represents a snapshot of the compositional variation within the laser induced plume,

[a]Department of Geology, University of Maryland, College Park, Maryland 20742, USA. E-mail: tangmyes@gmail.com; Fax: +1-301-405-3597; Tel: +1-240-374-3443
[b]NASA Goddard Space Flight Center, Greenbelt, Maryland 20771, USA
[c]Smithsonian Institution, Washington, DC 20013-7012, USA

† Electronic supplementary information (ESI) available. See DOI: 10.1039/c5ja00320b

and provides key information for characterizing elemental fractionation during particle formation processes.

Experimental

Laser ablation

A freshly polished section of the standard reference material NIST 610 (~400 parts per million by weight concentrations of most trace elements. Detailed compositional data are available at GeoReM: http://www.georem.mpch-mainz.gwdg.de/sample_query_pref.asp) was irradiated by a Photon Machines Analyte G2 excimer (ArF) laser ablation system at NASA Goddard Space Flight Center. This laser produces 193 nm wavelength radiation in 4 ns pulses at repetition rates up to 100 Hz. For this study, a laser spot with the following parameters was processed on the reference material: 110 μm spot diameter, 10 Hz repetition rate, 2.0 J cm^{-2} fluence, and 500 total shots.

Prior to irradiation, the sample chamber (helix cell) was purged with a He gas flow up to 2 L min^{-1} in order to evacuate any particulate contamination. During sample processing, however, the flow of helium was disengaged (*i.e.*, 0 L min^{-1} He) and the reference material was ablated under a static He atmosphere.

Secondary electron microprobe (SEM) imaging

Backscattered electron (BSE) imaging and Energy Dispersive Spectrometry (EDS) analysis were performed using a 7 kV electron beam with a 4.5 micron diameter and gaseous analytical detector (GAD) on the FEI Nova nanoSEM 600 instrument at the Smithsonian Institution. Low vacuum (1 mbar water vapor pressure) conditions allowed imaging and analysis of glass samples that were not conductively coated.

ToF-SIMS

Ion imaging and depth profiling were performed using the ION TOF GmbH IV TOF-SIMS instrument at the Smithsonian Institution. A primary 25 keV Bi^+ beam (pulsed current of 0.3 pA) was

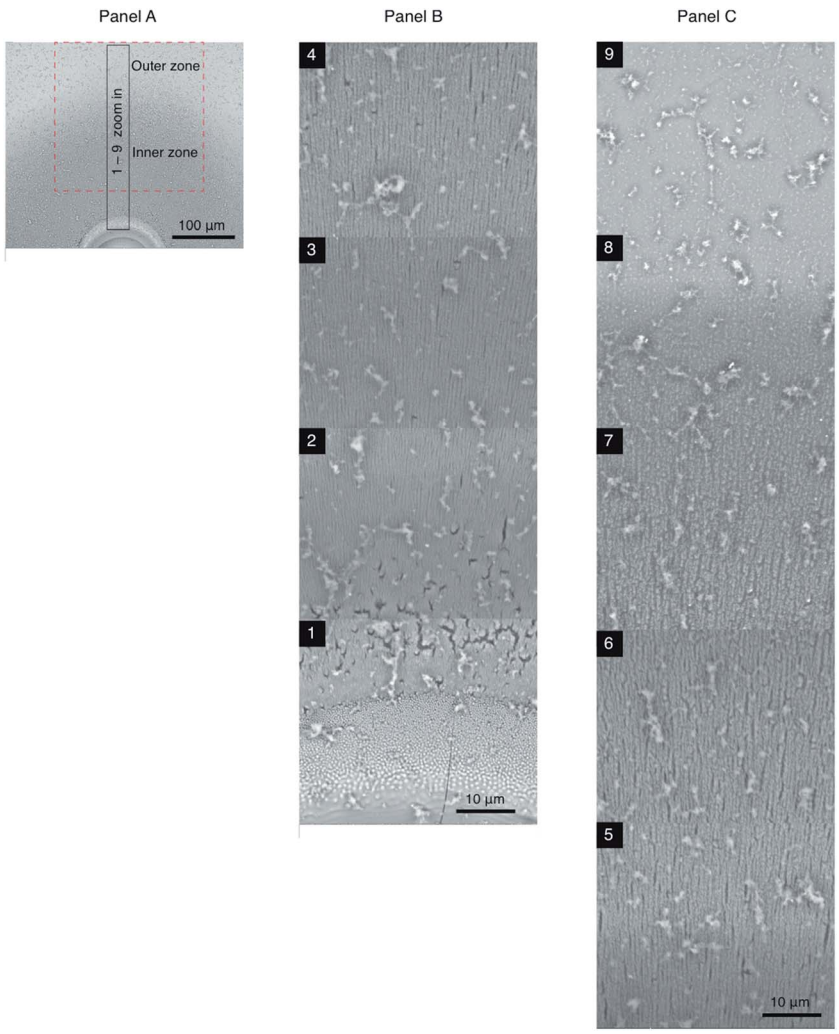

Fig. 1 BSE images of the condensate blanket adjacent to the laser crater. Panel A provides an overview of the condensate blanket, which can be broken down into well-defined inner and outer zones based on particle morphology. Panel B and C are zoom-in images of zones 1–9 (total length is 300 μm), each section representing approximately 40 μm × 35 μm and progressing away from the ablation site. The red dashed square in the left panel denotes the 250 × 250 micron area for ToF-SIMS imaging.

rastered over an area of 250 × 250 μm for 6000 seconds, producing 600 consecutive each scans with ~2 μm per pixel lateral resolution. To improve counting statistics we integrated every 40 scans to make an integrated scan, thus 15 integrated scans in total were made. Each integrated scan has a sputtering depth of ~3 nm for a total penetration depth of ~48 nm for the 6000 s scanning. This sputtering rate was estimated based on the sputtering rate obtained on silica glass, which is ~0.02 Å s^{-1} for a 500 × 500 μm^2 area.

Results and discussion

A distinct condensation blanket ~300 μm in diameter around the 110 μm laser crater is apparent in BSE images (Fig. 1(A)). The surface texture varies across the condensation blanket. The laser crater is surrounded by a narrow belt of beads that are 100 nm to 1 μm in diameter (Fig. 1(B), zone 1). Farther from the ablation site (zones 2–6), more fiber-like condensates can be seen extending towards the boundary of inner zoning at 200 μm from the crater (top of zone 6); individual particles cannot be resolved in this "fiber" zone. On the edge of the boundary (*e.g.*, Fig. 1(C), zones 5–7) are particle agglomerates of 10^2–10^3 nm, which show a clear preferred orientation. The surface area in the outer zone appears to be filled with smaller (<10 nm) condensates (*e.g.*, zones 8–9). The BSE images also reveal massive particle agglomerates (up to 10 μm) scattered throughout the surface covering both the laser pit ejecta blankets and remote areas of the sample (all zones). These agglomerates have a similar composition as NIST 610 glass based on EDS spectra, and thus were likely generated during laser ablation processing. For comparison, we provide a "control" SEM image of an area far (~5 mm away from the ablation site) from the laser crater (Fig. 2).

We used a ToF-SIMS instrument to produce ion images of an area that included representative regions of the two distinct zones of condensation blanket (Fig. 1, panel A). For ToF-SIMS data, we normalized all isotopes to ^{40}Ca; the less abundant ^{43}Ca is routinely used as an internal standard in LA-ICP-MS data reduction. It's worth noting that the X/Ca intensity ratios measured by ToF-SIMS do not reflect the accurate atomic ratios in the blanket. Calcium and other metals fractionate during sputtering due to different X–O bonding energies.[20–22] For our purpose, we focused on the relative X/Ca variation across the condensate blanket. Thus no external standard calibration was applied. Examples of the distributions of X/Ca ratios (X is an element other than Ca) in the first integrated scan are plotted in Fig. 3 (a complete set of integrated scans 2–15 are available in the ESI†). Similar to the textural variation across the condensate region, as revealed through BSE images, the ToF-SIMS images show compositional zonings (Fig. 3). For ^{7}Li, ^{9}Be, ^{11}B, ^{48}Ti, ^{51}V, ^{55}Mn, ^{56}Fe, ^{58}Ni, ^{65}Cu, ^{69}Ga, ^{87}Rb and ^{133}Cs, the inner zones are demarked by higher X/^{40}Ca intensity ratios; for ^{27}Al, ^{88}Sr and ^{138}Ba, the outer zones have higher X/Ca intensity ratios. ^{26}Mg shows less apparent fractionation across the frame. Sodium and potassium were also imaged by ToF-SIMS; however, both Na and K are major surface contaminants. In addition, Na oversaturated the detector. Therefore, Na and K data are not discussed here.

There are primarily two factors that may result in X/Ca variation: (1) laser induced elemental fractionation; and (2) topography induced matrix effects during ToF-SIMS analysis. The latter is a result of non-equilibrium sputtering. Generally, pre-sputtering can destroy surface structure and remove surface contaminants so as to avoid non-equilibrium sputtering effects. However, the non-equilibrium sputtering depth range is both matrix- and element-dependent. In this study, we did not apply pre-sputtering, but used the depth profiles to evaluate the non-equilibrium sputtering effect for each element. Relative differences (in%) in average X/Ca between the outer zone (farthest 100 μm from the ablation site) and inner zone (100 μm nearest the ablation site) for each integrated scan, as a function of sputtering depth (integrated scan number), are calculated in Fig. 4 and ESI.† If disproportionate enrichments or depletions in elemental abundances revealed by ToF-SIMS are solely due to topography changes across the condensation blanket, the normalized X/Ca zoning trends shown in these figures (*i.e.*, $X/Ca_{outer}/XCa_{inner}$) should "flatten out" with depth, as continuous sputtering is expected to resurface the sample and approach equilibrium sputtering conditions. Consequently, it is unlikely that our depth profiling penetrated through the condensate blanket, since the boundary between the inner and outer zoning neither disappeared nor changed its position in the ToF-SIMS images throughout the depth profile. Therefore our depth profile, sample the condensate blanket and should reflect the plume composition at the late stage of the ablation.

Among the geochemical proxies investigated here, Mg/Ca, Cs/Ca and Al/Ca may have non-equilibrium sputtering effects during early sputtering. For Mg, the Mg/Ca diff% between the outer and inner zonings continuously decreases with depth and reaches a plateau with a diff% of ~0% (Fig. 4), which suggests little Mg–Ca fractionation across the condensation blanket. For Cs, Cs/Ca in the outer zoning continuously decreases with sputtering depth while Cs/Ca in the inner zoning stays constant (Fig. 4), resulting in an increasing Cs/Ca diff% from integrated

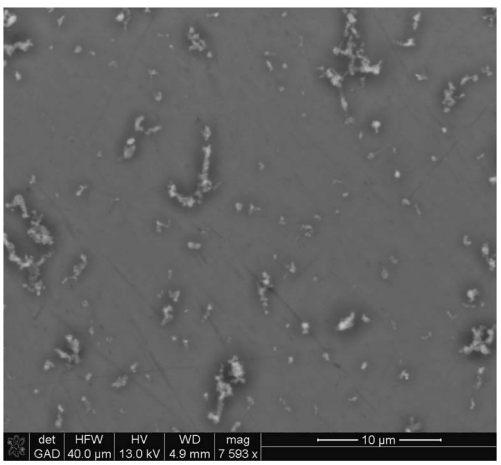

Fig. 2 Control BSE image of a polished section of the same NIST 610 sample after laser ablation, but located far (~5 mm) away from the ablation site. Note the reduced distribution of small particle condensates compared to those seen in the outer zone of the condensation blanket (Fig. 1C, zones 8–9).

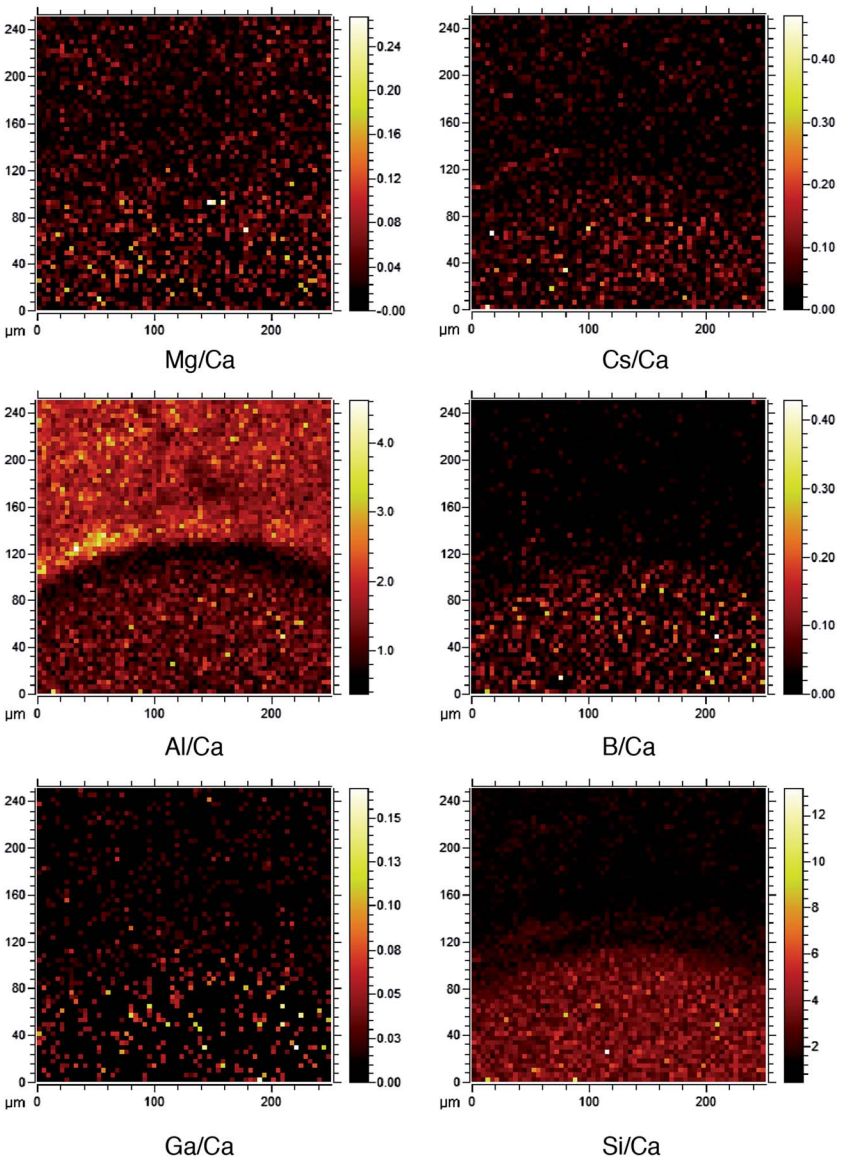

Fig. 3 Ca normalized Mg, Cs, Al, B, Ga and Si distributions across the condensate blanket (first integrated scan). Thermal scale reflects relative ion intensity from low (black) to high (white).

scan #1–5 followed by a plateau with a diff% of ~125%, indicating significant Cs–Ca fractionation induced by laser ablation. Al/Ca in the inner and outer zonings evolve in the opposite directions with no diff% plateau reached throughout the depth profile (Fig. 4); because of this, the fractionation between Al–Ca observed here likely represents only a lower bound on the actual fractionation between these elements. Although poorly resolved, Si/Ca and Cr/Ca appear to show decreased diff% between the outer and inner zones with sputtering depth. For the remainder, X/Ca diff% are significantly different from 0% with no resolvable systematic changes with sputtering depth, reflecting reproducible X–Ca fractionation of various sizes across the condensation blanket (see the ESI† for depth profiles of all elements analyzed here).

Laser induced elemental fractionation has been attributed to different chemical and physical properties of elements *e.g.*, volatility,[5–7,10,23] electronic structure,[6,11] *etc.*, resulting in preferential evaporation, ionization and condensation during laser ablation processes. Fig. 5 shows that volatile and transitional elements (Ni to Cs, 50% condensation temperature <1360 K) are mostly enriched in the inner zone while elements that are similarly refractory as Ca (V to Al, 50% condensation temperature >1360 K) can be enriched in either outer or inner zones, reflecting multiple factors controlling elemental fractionation. Multiple fractionation mechanisms can be further elucidated by comparing the contrasting fractionation directions between alkaline metals and alkaline earth metals (Fig. 6). Alkaline metals (period IA elements) are volatile and increasingly so with increasing atomic mass,[24] with the enrichment in alkaline metals increasing from Li to Cs in the inner zone (Fig. 6a). Alkaline earth metals (period IIA elements), however, share similar volatilities but transition from relative enrichments to

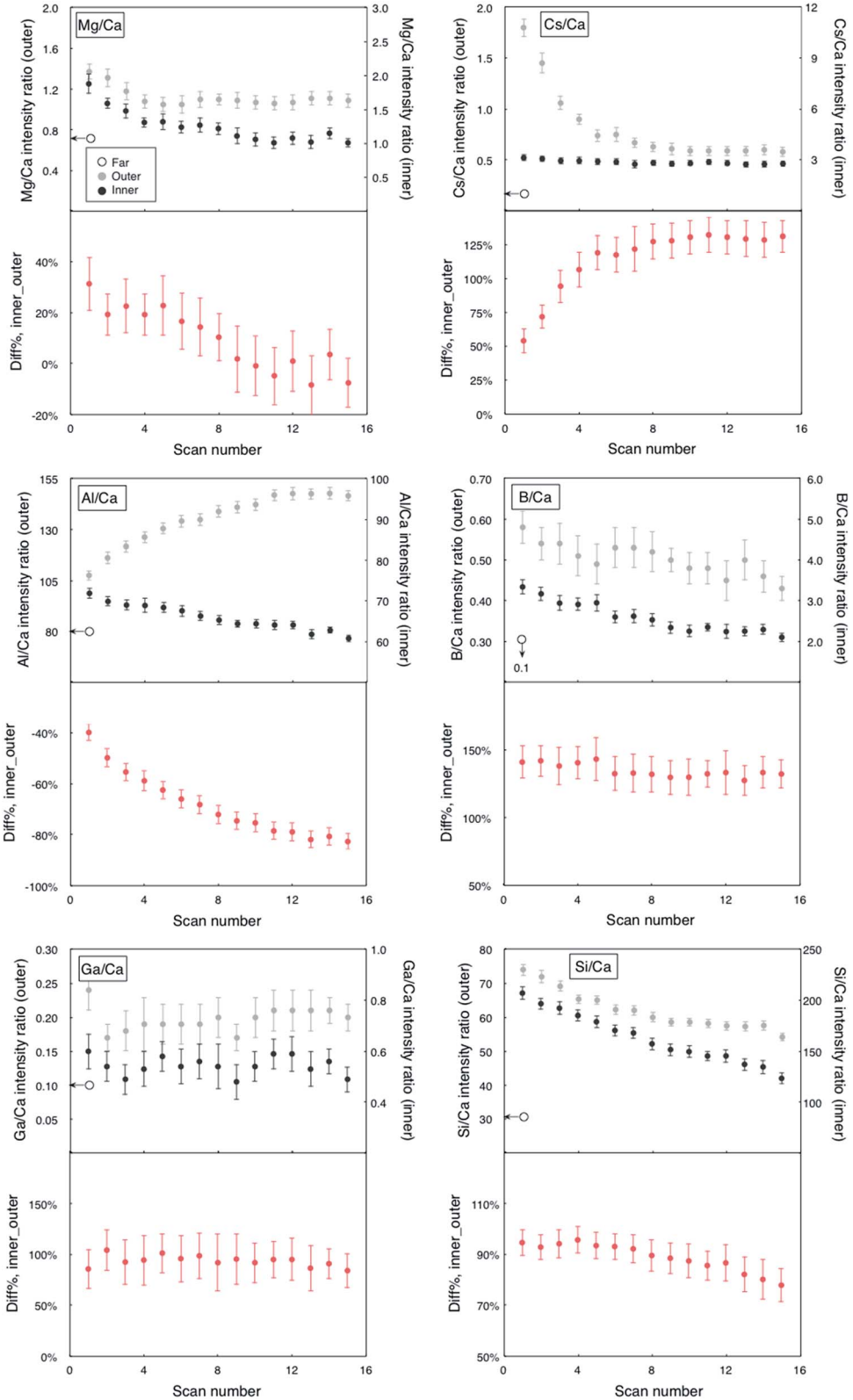

Fig. 4 Depth profiles of Mg, Cs, Al, B, Ga and Si, all normalized to Ca. A larger scan number on the *x*-axis corresponds to a deeper integrated scan. Note the dual *y*-axes in the uppermost plots. The gray dots represent the average X/Ca of the 100 μm outmost area (outer zone), the black dots the average X/Ca of the 100 μm innermost area (inner zone, nearest the ablation site), and the open circles represent the scan of a far area on the same NIST 610 glass after ablation. For each X/Ca panel, the diff% inner_outer is calculated as $(X/Ca_{inner} - X/Ca_{outer})/[(X/Ca_{inner} + X/Ca_{outer})/2] \times 100\%$. Error bars are $2\sigma_m$. See text for more explanation.

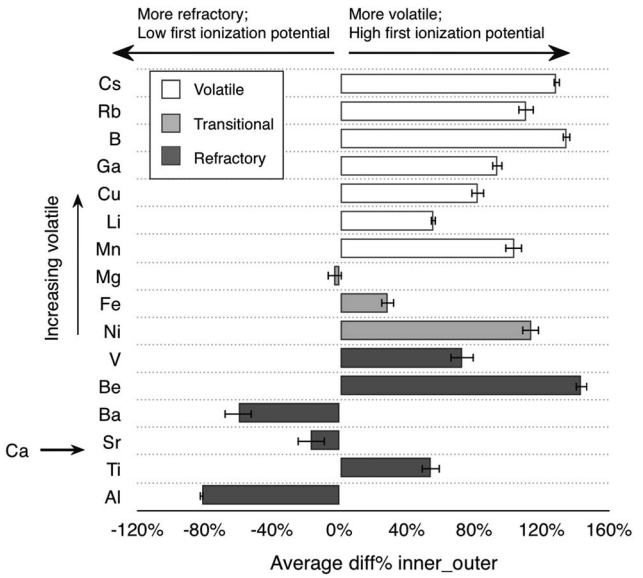

Fig. 5 Average X/Ca diff% between the inner and outer zonings. Negative values indicate relative enrichments in the outer zoning. Elements are defined as volatile, transitional or refractory based on condensation temperatures derived from Lodders (2003); note that these condensation temperatures are determined for a hydrogen atmosphere, while laser ablation was conducted in a helium atmosphere. Errors are $2\sigma_m$.

progressive depletions in between the inner zone as a function of first ionization potential (Fig. 6b), reflecting the control of electronic structure on the fractionation between alkaline earth metals. The opposite fractionation directions between alkaline metals and alkaline earth metals suggests the dominance of volatility effect over electronic structure effect on laser induced elemental fractionation (LIEF). The volatility control may also be responsible for the distinct fractionation behavior of Al compared with B and Ga since Al is enriched in the outer zoning while the more volatile B and Ga are both enriched in the inner zone (Fig. 4).

The compositional zonings around the laser crater are likely related to condensation behaviors and the spatial – temporal evolution of particle formation and deposition processes. Dynamically, during plasma plume initiation (10^{-10} s post-irradiation) the ascending material also undergoes laser-induced ionization at the sample surface during active irradiation with nanosecond (or longer) laser pulses.[25–27] Photothermally and photochemically activated materials irradiated with $\sim 10^9$ W cm^{-2} (*i.e.*, $\sim$2 J cm^{-2}, 4 ns, and 193 nm λ) rise from the sample surface and form a plasma plume, which in turn interacts with the incident laser irradiation and absorbs significant amounts (*circa* $\geq$50%) of laser energy that would otherwise couple with the sample, known as the plasma shielding effect.[2,28] The absorption of incident photons results in elevated temperatures (up to 10^4 K) and electron densities in the plume. During plume expansion, the temperature drops down and the excited species condense, aggregate and (eventually) form mostly sub-micron- and micron-sized particles. Within the expanding plume, temperature, pressure, electron density, and speciation (*e.g.*, ionization degree) are zoned.[25–27,29] Moreover, for plume residences time of 1 millisecond or longer, material in the pulse path will absorb the next incoming light pulse at 100 Hz repetition rates. As a result, the temporal and spatial scale condensation properties are expected to form condensates that compositionally vary as a function of distance from the ablation center. Although specifically developed for laser ablation of metallic substrates, Bogaerts and Chen's models[26,27] show that the spatial distribution of temperatures within the expanding plume is complex, and the plume develops a low temperature center after the laser pulse terminates. This may explain the relative enrichments of many volatile elements (*e.g.*, alkaline earth metals, B, *etc.*) in the inner zone of the condensation blanket. With condensation being the primary stage of particle formation (as opposed to less dominant evaporation processes, not discussed here), elemental fractionation during condensation corroborates the linkage between LIEF and particle size distribution.

Because elemental fractionation happens during laser plume condensation, achieving high accuracy and precision LA-ICP-MS data requires either complete mass transport and ionization in the ICP, or well matched internal standard element that fractionates in the same way as the unknown element during laser ablation of both the external standard and sample.[11,30] The former option requires well-designed laser ablation chamber and small aerosol particles produced by laser

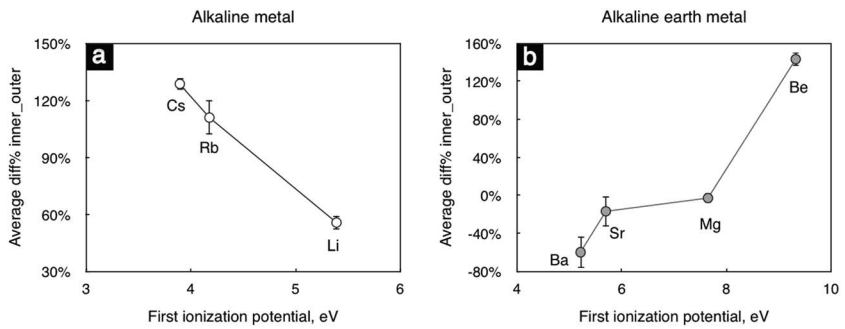

Fig. 6 Average X/Ca diff% between the inner and outer zones for alkaline and alkaline earth metal elements as a function of first ionization potential. Error bars are 2σ, and some are smaller than the markers.

ablation; the latter option requires dedicated analysis of only a limited range of elements with similar physicochemical properties (such as condensation temperature and first ionization potential) of the internal standard.

Finally, the findings of this study need to be placed into the context of active ablation with a He gas stream of 2 L min^{-1}, typical of modern laser ablation sampling for chemical and/or isotopic analyses. Under these conditions additional affects need to be considered, given plume trajectories of 10^4 m s^{-1} and strong gas flow velocities. Fractionation of volatile/refractory element species is likely to be enhanced, particularly for highly volatile elements Zn, Tl, Pb, In, Bi, Br and I. Horn *et al.* (2000)[31] observed correlation between element fractionation (U/Pb) and spot geometry (their Fig. 7) and suggested that the laser-induced elemental fractionation also reflected the relative efficiency of element transport for volatile *versus* refractory elements from the site of ablation to the ICP-MS.

Conclusions

(1) ToF-SIMS imaging reveals compositional zoning in the condensate blanket produced by ablation of NIST 610 glass with a pulsed (4 ns) ArF excimer (193 nm) laser system.

(2) The observed elemental fractionation is controlled by volatility as well as electronic structure (ionization potential), with volatility being the more influential factor; volatile and transitional elements (50% condensation temperature <1360 K) tend to be enriched in the inner zone relative to refractory elements, and low first ionization potential elements tend to be enriched in the inner zone relative to high first ionization potential elements.

(3) The elemental fractionation is associated with condensation and subsequent particle formation processes, during which the gradients in physical and chemical conditions result in uneven condensation within the plasma plume.

(4) ToF-SIMS imaging of laser condensate blanket provides a new approach to study the mechanisms of laser induced elemental and isotopic fractionation.

Acknowledgements

This project is funded by NSF grants EAR-0739006 and EAR-0948549. The first author also appreciates the support from the graduate school of the University of Maryland (Ann G. Wylie Fellowship). ToF-SIMS work (Yulia Goreva) was supported by NASA grant NNX14AF27G and funding from Deep Carbon Observatory. We thank editor Harriet Brewerton for handling our paper, and two anonymous reviewers for their comments and suggestions.

References

1 R. Arevalo Jr, in *Treatise on Geochemistry*, ed. H. D. H. K. Turekian, Elsevier, Oxford, 2nd edn, 2014, DOI: 10.1016/B978-0-08-095975-7.01432-7, pp. 425–441.
2 D. W. Bäuerle, *Laser Processing and Chemistry*, Springer, 2011.
3 M. Guillong, I. Horn and D. Gunther, *J. Anal. At. Spectrom.*, 2003, **18**, 1224–1230.
4 I. Horn, M. Guillong and D. Günther, *Appl. Surf. Sci.*, 2001, **182**, 91–102.
5 X. Mao, W.-T. Chan, M. Caetano, M. A. Shannon and R. E. Russo, *Appl. Surf. Sci.*, 1996, **96–98**, 126–130.
6 X. L. Mao, O. V. Borisov and R. E. Russo, *Spectrochim. Acta, Part B*, 1998, **53**, 731–739.
7 S. M. Eggins, L. P. J. Kinsley and J. M. G. Shelley, *Appl. Surf. Sci.*, 1998, **127–129**, 278–286.
8 J. Kosler, M. Wiedenbeck, R. Wirth, J. Hovorka, P. Sylvester and J. Mikova, *J. Anal. At. Spectrom.*, 2005, **20**, 402–409.
9 I. Kroslakova and D. Gunther, *J. Anal. At. Spectrom.*, 2007, **22**, 51–62.
10 M. Tang, W. F. McDonough and R. J. Arevalo, *J. Anal. At. Spectrom.*, 2014, **29**, 1835–1843.
11 F. E. Jenner and H. S. C. O'Neill, *Geochem., Geophys., Geosyst.*, 2012, **13**, Q03003.
12 J. Koch, A. von Bohlen, R. Hergenroder and K. Niemax, *J. Anal. At. Spectrom.*, 2004, **19**, 267–272.
13 M. Guillong and D. Gunther, *J. Anal. At. Spectrom.*, 2002, **17**, 831–837.
14 H.-R. Kuhn and D. Günther, *Anal. Chem.*, 2003, **75**, 747–753.
15 J. Mikova, J. Kosler, H. P. Longerich, M. Wiedenbeck and J. M. Hanchar, *J. Anal. At. Spectrom.*, 2009, **24**, 1244–1252.
16 M. Guillong, H.-R. Kuhn and D. Günther, *Spectrochim. Acta, Part B*, 2003, **58**, 211–220.
17 S. H. Jeong, O. V. Borisov, J. H. Yoo, X. L. Mao and R. E. Russo, *Anal. Chem.*, 1999, **71**, 5123–5130.
18 R. Hergenroder, *J. Anal. At. Spectrom.*, 2006, **21**, 517–524.
19 T. Stephan, *Planet. Space Sci.*, 2001, **49**, 859–906.
20 T. Henkel and J. Gilmour, in *Treatise on Geochemistry*, ed. H. D. H. K. Turekian, Elsevier, Oxford, 2nd edn, 2014, DOI: 10.1016/B978-0-08-095975-7.01431-5, pp. 411–424.
21 T. R. Ireland, in *Treatise on Geochemistry*, ed. H. D. H. K. Turekian, Elsevier, Oxford, 2nd edn, 2014, DOI: 10.1016/B978-0-08-095975-7.01430-3, pp. 385–409.
22 J. C. Vickerman, J. C. V. D. Briggs and D. Briggs, *ToF-SIMS: Materials Analysis by Mass Spectrometry*, IM Publications, 2013.
23 C. Liu, X. L. Mao, S. S. Mao, X. Zeng, R. Greif and R. E. Russo, *Anal. Chem.*, 2003, **76**, 379–383.
24 K. Lodders, *Astrophys. J.*, 2003, **591**, 1220.
25 A. Bogaerts and Z. Chen, *J. Anal. At. Spectrom.*, 2004, **19**, 1169–1176.
26 A. Bogaerts and Z. Chen, *Spectrochim. Acta, Part B*, 2005, **60**, 1280–1307.
27 Z. Chen and A. Bogaerts, *J. Appl. Phys.*, 2005, **97**, 063305.
28 R. E. Russo, X. Mao, H. Liu, J. Gonzalez and S. S. Mao, *Talanta*, 2002, **57**, 425–451.
29 A. Bogaerts, Z. Chen, R. Gijbels and A. Vertes, *Spectrochim. Acta, Part B*, 2003, **58**, 1867–1893.
30 M. Gaboardi and M. Humayun, *J. Anal. At. Spectrom.*, 2009, **24**, 1188–1197.
31 I. Horn, R. L. Rudnick and W. F. McDonough, *Chem. Geol.*, 2000, **164**, 281–301.

